A general workflow for characterization of nernstian dyes and their effects on bacterial physiology

Biophysical Journal
Article

Biophysical Society

A General Workflow for Characterization of Nernstian Dyes and Their Effects on Bacterial Physiology

Leonardo Mancini,[1] Guillaume Terradot,[1] Tian Tian,[2] YingYing Pu,[2] Yingxing Li,[2] Chien-Jung Lo,[3] Fan Bai,[2] and Teuta Pilizota[1,*]

[1]Centre for Synthetic and Systems Biology, University of Edinburgh, Edinburgh, United Kingdom; [2]Biomedical Pioneering Innovation Center, School of Life Sciences, Peking University, Beijing, China; and [3]Department of Physics and Graduate Institute of Biophysics, National Central University, Jhongli, Taiwan, Republic of China

ABSTRACT The electrical membrane potential (V_m) is one of the components of the electrochemical potential of protons across the biological membrane (proton motive force), which powers many vital cellular processes. Because V_m also plays a role in signal transduction, measuring it is of great interest. Over the years, a variety of techniques have been developed for the purpose. In bacteria, given their small size, Nernstian membrane voltage probes are arguably the favorite strategy, and their cytoplasmic accumulation depends on V_m according to the Nernst equation. However, a careful calibration of Nernstian probes that takes into account the tradeoffs between the ease with which the signal from the dye is observed and the dyes' interactions with cellular physiology is rarely performed. Here, we use a mathematical model to understand such tradeoffs and apply the results to assess the applicability of the Thioflavin T dye as a V_m sensor in *Escherichia coli*. We identify the conditions in which the dye turns from a V_m probe into an actuator and, based on the model and experimental results, propose a general workflow for the characterization of Nernstian dye candidates.

SIGNIFICANCE The phospholipid bilayer of a biological membrane is virtually impermeable to charged molecules. Much like in a rechargeable battery, cells harness this property to store an electrical potential that fuels life reactions but also transduces signals. For the case of bacteria, which are small in size and possess a stiff cell wall, arguably the most popular approach to measuring membrane voltage are Nernstian probes, which accumulate across the bacterial membrane according to the Nernst equation. This study characterizes the undesired effects Nernstian probes can have on cell physiology, which can be crucial for the accurate interpretation of experimental results. Using mathematical modeling and experiments, the study provides a general, simple workflow to characterize and minimize these effects.

INTRODUCTION

Living cells maintain an electric potential difference (V_m) across the plasma membrane that acts like a capacitor. This is achieved by active transport of ions:

$$V_m = F \times \frac{Q_{in}}{C}, \quad (1)$$

where Q_{in} is the intracellular charge (in moles), C the membrane capacitance, and F the Faraday constant. Membrane potential stands at the basis of fundamental biological processes such as signal transduction and energy production (1,2). For the latter, V_m adds up to the chemical potential of protons arising from their concentration difference across the membrane to result in the proton electrochemical gradient, the so-called proton motive force (PMF). The PMF drives numerous cellular processes, most notably the production of ATP (2), import of nutrients or osmolites (3–6), and rotation of the bacterial flagellar motor (BFM) (7), and it is necessary for cell division (8).

Submitted April 12, 2019, and accepted for publication October 18, 2019.

*Correspondence: teuta.pilizota@ed.ac.uk

Guillaume Terradot and Tian Tian contributed equally to this work.

Editor: Amy Palmer.

https://doi.org/10.1016/j.bpj.2019.10.030

The notion that V_m lies at the very basis of life motivated decades long efforts to measure it (9). The first direct technique dates to 1939 and relies on the mechanical insertion of microelectrodes into squid giant axons (10). The method led to the development of the patch-clamp technique, which advanced the understanding of neuron signal transduction (11–13). However, the applicability of microelectrodes for the measurement of bacterial V_m is limited, owing to the small size of the organisms and the presence of the cell wall (14,15). Some of the subsequently developed methods overcome such limits with the use of molecular sensors (16), grouped into two categories: conformational-change-based sensors and Nernstian sensors. The former are static molecules or proteins that sit inside the membrane or in its close proximity and change conformation or electron distribution in response to changes in V_m, which, in turn, affect the optical properties of the chromophores (17–19). Here, we focus on the latter, the Nernstian sensors, and on the parameter range in which they serve as V_m indicators, using *E. coli* as the model organism.

Nernstian sensors are charged molecules that can diffuse across the biological membranes and distribute according to the Nernst equation:

$$V_m = \frac{RT}{zF}\ln\left(\frac{c_{out}}{c_{in}}\right), \tag{2}$$

where R, T, z, F, c_{out}, and c_{in} denote, respectively, gas constant, temperature, valence of the charged molecule, Faraday's constant, and external and internal concentrations of the charged molecule. For a measurement to be attained, these molecules need to emit a signal that is a proxy for their number. Therefore, Nernstian V_m dyes are usually radiolabeled or fluorescent molecules (16,20), and V_m is calculated from Eq. 2 by measuring the cytoplasmic (c_{in}) and the external dye concentrations (c_{out}) (21).

However, Nernstian dyes are used in complex biological systems, and a number of factors can be responsible for an incomplete adherence to a fully Nernstian behavior. In Fig. 1, we give a cartoon representation of the tradeoffs imposed on a Nernstian dye by plotting the dye intensity inside *E. coli*'s cytoplasm against the time. The chosen dye concentration should be such that the signal is sufficiently above the background (ΔI is sufficiently large). Yet, with increasing dye concentration, a cell's V_m is more likely to be affected by the dye. This caveat is inherent to positively charged dyes because these directly lower V_m and more so at higher concentrations (22). The first requirement for a Nernstian dye is thus the existence of a range of concentrations that give sufficient signal without extensively affecting the V_m. Likewise, cellular processes should not interfere with the Nernstian behavior of the dye, for example, by actively importing or exporting it. Instead, the dye should be able to diffuse across the membrane, and its diffusion constant will determine the time it takes for the dye to equilibrate across the membrane in agreement with Eq. 2 (τ_{eq} in Fig. 1). All phenomena that occur quicker than τ_{eq} are beyond the dye's temporal resolution, and all the measurements taken before τ_{eq} do not faithfully report V_m. Lastly, different dyes bind to the membrane or form aggregates to a different extent (21,23)). However, as long as the dyes do not self-quench at any point (24) or undergo signal enhancements, a constant and well-defined correlation function between the free dye concentration and the signal can be obtained, thus enabling quantitative V_m measurements (most commonly, this is done by separating the signal from the free and bound dye with careful calibration (21,23)).

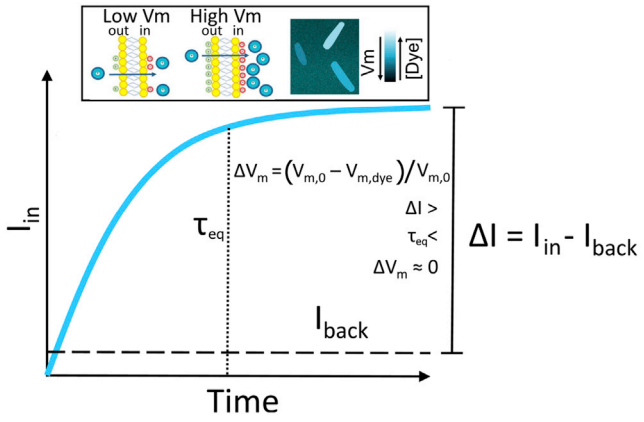

FIGURE 1 A schematic plot of a Nernstian dye equilibration curve. Equilibration time, τ_{eq}, is defined as the time at which the dye internalized by the cell, dye I_{in}, reaches 90% of its final value. $V_{m,0}$ and $V_{m,dye}$ indicate the membrane potential before and after the addition of the dye, respectively. I_{back} is the fluorescence intensity of the background. Inset: cartoon showing the mechanism of accumulation of cationic dyes, which accumulate more in cells with a more negative V_m. To see this figure in color, go online.

To summarize, to be used as an ideal Nernstian sensor, a cationic dye should 1) give a sufficiently high signal without affecting cell's V_m; 2) diffuse through the membrane with τ_{eq} on the order of minutes; 3) stay inert, despite being charged, and not form bonds or in any way interact with the cell; and 4) have constant signal per molecule. Yet, when using such dyes, these requirements are rarely assessed in a systematic manner before measurements commence. In this work, we identify a workflow that should be adopted, for a given choice of the dye, organism, and external environment, to identify the parameter range in which Nernstian dyes act as sensors rather than actuators, i.e., molecules that actively decrease or increase the V_m. We start with a mathematical model that helps us understand relationships and define tradeoffs between dye working concentration and signal intensity, equilibration time, and V_m perturbation. We then show how the identified workflow can be used to benchmark new Nernstian dyes by characterizing the recently reported dye Thioflavin T (ThT) used in *Bacillus subtilis* (25) for use in *E. coli*. We describe the

physiological range in which ThT enables V_m sensing in *E. coli*, and, in the range in which we find it turns into an actuator, we investigate the mechanistic reasons. Our workflow can be applied to the characterization of other Nernstian dyes and provide novel insights for the established ones.

METHODS

Bacterial strains

All experiments in which no mutation is explicitly indicated were carried out in the MG1655 strain. For the BFM speed assay, we used MG1655 carrying the FliC-sticky mutation from (26). *ΔtolC* mutants were obtained from the Keio collection (27). Kanamycin resistance of the Keio deletion strain was removed via one-step inactivation with the plasmid pCP20 (28). Kanamycin resistance inactivation and elimination of the pCP20 plasmid were confirmed via kanamycin (50 μg/mL), chloramphenicol (31 μg/mL), and ampicillin (100 μg/mL) sensitivity tests. Both the strain carrying the *ΔtolC* mutation and MG1655 wild type (WT) were transformed with plasmid pTP20-mKate2 (Fig. S1) for cytoplasmic volume measurements. pTP20-mKate2 contains the red fluorescent protein mKate2 and the ribosomal binding site of mCherry. The plasmid was constructed as follows: the backbone from pWR20 (29) and the sequence containing the ribosomal binding site of mCherry and mKate2 were PCR-amplified. The products were purified, cleaved with the restriction enzymes AvrII and NotI (New England Biolabs, Hitchin, UK), and ligated using T4 DNA ligase (Promega, Chilworth, UK). Chemically competent cells were transformed with the ligation mixes, and transformants were confirmed by colony PCR and subsequently sequenced. A map of the plasmid and the primers are given in Fig. S1 and Table S1. All the strains used in the study are summarized in Table S2.

Bacterial growth conditions

Cells for fluorescence microscopy were grown from an overnight culture by diluting it 1:80 times in Luria-Bertani broth (0.5% yeast extract, 1% Bacto Tryptone, 1% NaCl). The culture was shaken at 220 rpm at 37°C and harvested at OD_{600} = 0.3–0.5. Cells were then washed into fresh LB or MM9 + glucose medium (50 mM Na_2HPO_4, 25 mM NaH_2PO_4, 8.5 mM NaCl, 18.7 mM NH4Cl, 0.1 mM $CaCl_2$, 1 mM KCl, 2 mM $MgSO_4$, 1× modified Eagle's medium essential amino acids (Gibco, Paisley, UK), and 0.3% glucose). For the simultaneous BFM speed and ThT fluorescence measurements, cells were grown from an overnight culture by diluting it 1:80 times in TB (1% Bacto Tryptone, 0.5% NaCl) at 200 rpm and 30°C. Cells were harvested at OD_{600} = 0.8 as before (30) and washed into fresh MM9 via centrifugation. Growth curves in the presence of ThT were obtained in a Spectrostar Omega microplate reader (BMG, Ortenberg, Germany) using a flat-bottom 96-well plate that was covered with a lid during the experiments (Costar, Glasgow, UK). Each well contained 200 μL of growth media, either MM9 + glucose or MM9 + glycerol (50 mM Na_2HPO_4, 25 mM NaH_2PO_4, 8.5 mM NaCl, 18.7 mM NH4Cl, 0.1 mM $CaCl_2$, 1 mM KCl, 2 mM $MgSO_4$, 1× modified Eagle's medium essential amino acids (Gibco), and 0.3% glycerol), and was inoculated with 2 μL (1:100 dilution) of an overnight culture and a given concentration of ThT. Plates were grown at 37°C with 300 rpm shaking (double orbital mode). ThT (Acros Organics, Loughborough, UK) solutions were prepared from a 10 mM stock of ThT in water made at least monthly and stored at 4°C in the dark.

Fluorescence microscopy

Imaging was carried out in a custom-built microscope with a 100× oil immersion objective lens (Nikon, Tokyo, Japan) and a neutral white LED as a source of illumination (Cairn Research, Faversham, UK), and images were taken with an iXon Ultra 897 EMCCD camera (Andor, Belfast, UK) (31,32). ThT fluorescence was measured with ZET436/20× and ET525/40 m, and mKate2 and propidium iodide (PI) fluorescence with ET577/25× and ET632/60 m (Chroma Technology, Bellows Falls, VT) excitation and emission filters, respectively. Images were taken at 1 min intervals, exposure time was 50 ms and Andor camera gain 25. We note that ThT undergoes a spectral shift and intensity increase when highly concentrated or when spatially constricted, either by binding to amyloid fibrils or by viscosity (33–35). Our choice of filters aims at minimizing these effects and the damage that shorter wavelengths cause to *E. coli* (36). Cells were imaged in a custom-built flow cell (Fig. S2; (26)) and attached to the coverslip surface as before (26,30). Briefly, 1% poly-L-lysine (Sigma-Aldrich, Gillingham, UK) is flushed through the flow cell and washed with 3–5 mL of growth media after 10 s. Polystyrene particles (beads) with a diameter of 1 μm (Bangs Laboratories, Fishers, IN), were delivered into the flow cell and allowed to attach to the coverslip surface. After 10 min, unattached beads were flushed away with 1–2 mL of growth media. Next, 200 μL of cells were delivered to the flow cell and allowed to attach for 10–30 min, after which the unattached cells were removed with 1 mL of growth medium. 10 μM ThT in growth media was delivered with a peristaltic pump (Fusion 400; Chemyx, Stafford, TX) using 50 μL/min flow rate while imaging. We deliver 5 μM of PI stain (MP Biomedicals, Loughborough, UK) in the same way. 5 mM PI stock solution (in water) was stored at 4°C in the dark. Images were stabilized in x, y, and z positions using a bead attached to the coverslip and back-focal-plane interferometry (29,37). Cells grow attached to the poly-L-lysine surface with expected growth rates (given the medium), as previously reported (38) and seen in Videos S1 and S2.

Motor speed measurements

Single motor speeds were measured as before (26,30). Briefly, we sheared flagellar filaments by passing them through two syringes with narrow-gauge needles (26 gauge) connected by plastic tubing. The cell attachment protocol was as above, except 0.5 μm beads (Polysciences, Warrington, PA) were delivered after cell attachment allowing them to attach to filament stubs. Motor speed was measured during continuous flow that delivered MM9 + glucose medium supplemented with 10 μM ThT. Back-focal-plane interferometry setup and recording conditions are as before (30).

Data analysis

Motor speed traces

Raw traces of the position of the bead attached to the filament stub were analyzed by a moving-window discrete Fourier transform as in (30). From the obtained motor speed traces, DC frequency (50 Hz) was removed, speeds lower than 5 Hz were ignored, and subsequently a median filter (window size 11) was applied (26). We note that we use a WT strain for which the BFM can change rotational direction, which appears as a negative speed after application of the moving-window Fourier transform. However, for the purpose of the PMF measurements, these short intervals can be disregarded, and we only show the speed values above 0 Hz.

Fluorescence images

The image analysis was carried out with custom-written software. From fluorescence images, rectangles containing "flat" cells, i.e., cells that are uniformly attached to the coverslip surface, as well as background rectangles within each cell-containing rectangle, were manually selected (29,37). The edge of the cell was identified within the cell-containing rectangle by applying a global threshold via the Otsu's method (39). Total cells' intensity values were obtained by summing up and averaging pixel belonging to the cells. Values obtained from the background rectangles at the time points

when ThT was loaded in the channel but cells had not taken it up yet were subtracted from the cell intensity values. The beads used for image stabilization stain easily with ThT and were used as a point of reference for dye entry (which, in our case, occurred 7–10 min from the start of imaging). We show fluorescence intensity traces that start at the point of ThT entry but note that cells were exposed to fluorescence illumination in the 7–10 min interval before. For the low fluorescence values characteristic of the early stages of dye equilibration, our script fails to identify cells, in which case we linearly interpolate values between two closest events of successful cell identification. Cell area was measured from intensity profiles, by normalizing them and counting the pixels above 30% of maximum intensity as described previously (29,37).

Plate reader data

Individual growth curves were analyzed with the software deODorizer from (40). To extract the maximum growth rate, three or more repeats in the same condition were aligned by the chosen OD value (usually OD $\sim$ 0.4) using the growth curve that reached it first (in the given condition). The maximum growth rates given in Fig. 3 *C* were normalized by the maximum growth rate in $[\text{Dye}]_{out} = 0$ condition.

RESULTS

Mathematical model of Nernstian dye's behavior defines its working parameter range

To predict and understand the mutual effects of dye concentration and cell physiology, we turn to a mathematical model. We assume that the cytoplasmic and extracellular liquids are electrical conductors separated by a membrane, which we treat as a parallel-plate capacitor (Eq. 1; (41,42)). We model the membrane as a single lipid barrier and do not distinguish between the inner and outer membrane of *E. coli*. In the Supporting Materials and Methods, we discuss a more detailed model that includes both membranes and allows for the existence of a small V_p across the outer membrane in addition to the V_m across the inner membrane. We account for four types of charge carriers and assume that all are monovalent to simplify the model without altering the results with respect to V_m dye behavior: 1) negatively charged molecules to which the membrane is close to nonpermeable, denoted Y (this includes surface charges on the inside of the membrane); 2) cationic species actively pumped outward, denoted C^+; 3) anionic species, which equilibrate across the membrane A^-; and 4) cationic species that equilibrate across the membrane (playing the part of a cationic dye). Thus, Q_{in} is

$$Q_{in} = V_{cell} \times \underbrace{\sum_x z_x [x]_i}_{\text{General Form}}$$

$$= V_{Cell} \times \underbrace{\left([Dye]_{in} + [C^+]_{in} - [A^-]_{in} - [Y]_{in}\right)}_{\text{This manuscript}}, \quad (3)$$

where V_{cell} is the intracellular volume, z_x the valency of species x, and $[x]_i$ its intracellular concentration (we only consider $z_x = \pm 1$). The extracellular concentrations and $[Y]_{in}$ are constants set by the initial conditions (we assume that the cell does not affect the ionic composition of its environment, and we treat $[Y]_{in}$ as unable to cross the membrane). We also assume that the cell uses only one type of pumps for cations, and note that $[Dye]_{in}$ and $[Dye]_{out}$ are experimentally determined from fluorescence intensity signal (see Fig. 6 later in the text).

The charge separation, and thus V_m, is achieved in the close proximity of the bilayer so that the rest of the cell's cytoplasm stays electroneutral (42,43) and in two ways: first, by pumping C^+_{in} outwards and thus creating a negatively charged intracellular environment, and second, by maintaining $[Y]_{in}$. Pumping C^+ outwards against its electrochemical gradient requires free energy, which we consider a constant and label ΔG_E (where $\Delta G_E < 0$). For example, in the case of a proton/ion antiporter with 1:1 exchange stoichiometry, the free energy is the PMF itself; for a similar antiporter with 2:1 proton/ion stoichiometry, it is 2$\times$ PMF; and for ATP hydrolysis, ΔG_E is the amount of work given by hydrolyzing one ATP.

The rate at which C^+ is pumped out of the whole cell, given in mol/m^3/s, is

$$j_P = k_P \times \left(1 - e^{\Delta G_P/(RT)}\right), \quad (4)$$

where k_P is a function that describes the specifics of the transport mechanism by a given pump; here, we keep it a constant. ΔG_P depends on the electrochemical potential of the pumped cation (ΔG_{C^+}) and ΔG_E. Therefore, the rate of pumping (positive flux means C^+ is extruded) depends on the intracellular ionic composition via V_m and $[C^+]_{in}$:

$$\Delta G_P = \Delta G_E - \Delta G_{C^+}, \quad (5)$$

$$\Delta G_{C^+} = F \times V_m + RT \times \ln\left(\frac{[C^+]_{in}}{[C^+]_{out}}\right). \quad (6)$$

Note that for the pump to move C^+ outward, $j_P > 0$, and consequently $\Delta G_E < \Delta G_{C^+}$, i.e., the free-energy-providing reaction has to be able to overcome the electrochemical gradient of the C^+. The chosen functional dependency of j_P gives the simplest pump kinetics, sufficient for our purpose, that can be expanded to include more complex pumping scenarios (44).

Finally, the dye, the anion, and the cation leak through the membrane (positive flux means x is moved inward) at the rate

$$j_{L,x} = k_{L,x} \times \left(1 - e^{\Delta G_x/(RT)}\right), x \in \{Dye, C^+, A^-\}, \quad (7)$$

$$\Delta G_x = F \times V_m + RT \times \ln\left(\frac{[x]_{in}}{[x]_{out}}\right). \quad (8)$$

Similarly to k_P, $k_{L,x}$ is a function whose shape depends on the mechanisms by which an ion leaks across the *E. coli* membrane, which, in turn, depends on the electrostatic potential at a position z within the membrane, $V(z)$. To the best of our knowledge, $V(z)$, and consequently $dV(z)/dz$, is not known for *E. coli*. Therefore, we chose Eyring's model, which has been verified for cationic leakage across the mitochondrial membrane (45) and that assumes $V(z)$ abruptly changes in the middle of the lipid bilayer such that $dV(z)/dz = 0$ everywhere but at the geometrical middle of the membrane, where $dV(z)/dz = V_m$ (46). We then have

$$k_{L,x} = \frac{S_{cell}}{V_{cell}} \times P_x \times [x]_{out} \times e^{-\frac{F \times V_m}{2 \times RT}}, \text{with } x \in \{Dye, C^+, A^-\}, \quad (9)$$

where S_{cell} denotes the cell's surface area and P_x the permeability of the membrane for $x \in \{Dye, C^+, A^-\}$ (obtained by assuming the solubility-diffusion model (47)).

At steady state, *Dye* and A^- equilibrate across the membrane according to the Nernst equation ($d[Dye]_{in}/dt = j_{L,Dye} = 0 \Leftrightarrow \Delta G_{Dye} = 0$, leading to Eq. 2), whereas for the monovalent cation, $d[C^+]_i/dt = 0 \Leftrightarrow j_{L,C^+} = j_P$. Next, we introduce a new variable ("pump-leak ratio"), defined as

$$\rho = k_P / k_{L,C^+} = k_P \times \frac{V_{cell}}{S_{cell} \times P_{C^+} \times [C^+]_{out}} \times e^{\frac{F \times V_m}{2 \times RT}}, \quad (10)$$

and rewrite the steady-state condition for C^+ as

$$\left(1 - e^{\Delta G_{C^+}/(RT)}\right) = \rho \times \left(1 - e^{\left(\Delta G_E - \Delta G_{C^+}\right)/(RT)}\right). \quad (11)$$

Given a certain extracellular composition ($[Dye]_{out}$, $[C^+]_{out}$, and $[A^-]_{out}$) and taking into account that $[Dye]_{in}$ and $[A^-]_{in}$ are defined by the Nernst equation at steady state, Eq. 11 gives us a unique solution for steady-state V_m for a set of $\{[Y]_{in}, \rho, \Delta G_E\}$ values while reducing the number of computational steps needed to reach it (see also the later paragraph describing computational steps of the model further).

We note from Eq. 11 that changing the functional dependency of k_{L,C^+} or k_P does not affect how the steady-state $V_{m,0}$ depends on ρ. However, the dynamics of dye equilibration and the steady-state potential after addition of the dye, relative to the steady-state potential in absence of the dye ($\Delta V_m = (V_{m,0} - V_{m,Dye})/V_{m,0}$), do. For example, had we assumed that the mechanism by which the ions leak across the *E. coli* membrane is better described by the Goldman-Hodgkin-Katz flux equation for $k_{L,x}$ (48), we would have obtained a slightly different dye equilibration profile (Fig. S3). However, the conclusions we reach based on our model predictions will not change because we are interested in the changes of the intracellular dye concentration dynamics at different extracellular dye concentrations, $V_{m,0}$ or P_{Dye}. These partial derivatives of the intracellular dye concentration are invariant to the choice of $k_{L,x}$ and k_P.

Having constructed the model, we obtain the computational data in Fig. 2 in two steps. In the first step, we allow the oridinary differential equation (ODE) system described by Eqs. S20 and S21 to reach the steady state ($V_{m,0}$) for a three-dimensional grid of $\{[Y]_{in}, \rho, \Delta G_E\}$. We note that in this step, we do not need to specify cation permeability nor the rate function for leakage k_{L,C^+} because we define the values of ρ, which is the ratio of the two ($\rho = 0$ for the anion and the dye). We then use the obtained $V_{m,0}$ as the initial condition for the second step of the numerical experiment, which requires us to specify 1) the rate function for leakage (Eq. 9), 2) the permeability of the membrane to the dye P_{Dye}, and 3) the concentration of the dye in the extracellular space $[Dye]_{out}$, which does not affect the cation pumping rate in our model.

To explore the tradeoffs imposed on a Nernstian dye (Fig. 1), we first look at the choice of the working concentration. Increasing the [*Dye*] gives better signal/noise ratio but can affect $V_{m,0}$, as depicted in Fig. 2 *A*. For a fixed $V_{m,0}$, $[Y]_i$, and ΔG_E, changing the external dye concentrations ($[Dye]_{out}$) improves the signal/noise ratio and shortens τ_{eq} but, at the same time, increasingly depolarizes the membrane. The extent by which ΔV_m drops does not solely depend on the $[Dye]_{out}$ but also on the initial $V_{m,0}$. Fig. 2 *B* shows dye equilibration profile for a fixed $[Dye]_{out}$ but for different $V_{m,0}$, indicating that highly polarized cells are more susceptible to V_m loss. Apart from the value of $V_{m,0}$, ΔV_m will also depend on the charged permeable and nonpermeable species that are generating it, as shown in Fig. S4. If a given $V_{m,0}$ value is generated in the presence of a higher concentration of charged, impermeable intracellular species or at a higher energetic cost, ΔV_m will increase for the same $[Dye]_{out}$. Thus, the extent to which a given [*Dye*] becomes an actuator and affects the ΔV_m is context-dependent, and the dye working concentration should be determined for each specific physiological condition. Additionally, Fig. 2 *A* shows that increasing $[Dye]_{out}$ shortens τ_{eq}, but only when $V_{m,0}$ is affected, as seen in Fig. S5.

Lastly, we look at the dye equilibration profile for different permeabilities of the membrane to the dye (P_{Dye}) in Fig. 2 *C* and show that for higher P_{Dye}, the same concentration of the dye lowers $V_{m,0}$ more. Fig. S4 shows τ_{eq} as a function of P_{Dye} for different $V_{m,0}$.

The working concentration of Nernstian dye ThT for *E. coli* is in μM range

Guided by the model predictions, we devise an experimental workflow for assessing the parametric range in which a candidate cationic dye behaves like an ideal Nernstian sensor. We choose ThT for the purpose; it has recently been used as a V_m dye in *B. subtilis* (25), but it has not

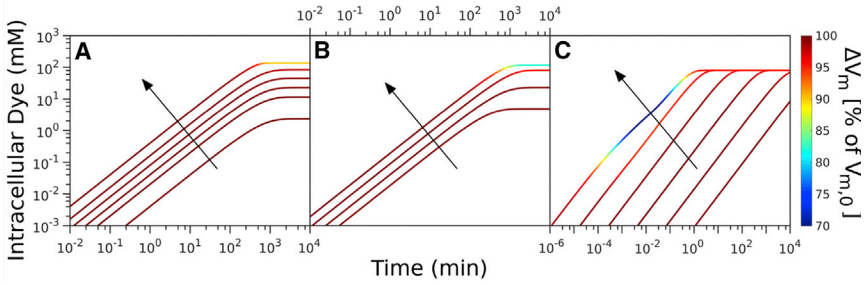

FIGURE 2 Computational data describing the parameter landscape associated with cationic dye usage as Nernstian sensors. (*A*) $V_{m,0} = -140$ mV, $Y_i = 150$ mM, $I_{Na} = 210$ mV. Intracellular dye concentration as a function of time is shown for extracellular dye concentrations 10, 50, 100, 200, 400, and 1000 μM. The arrow indicates increasing $[Dye]_{out}$. (*B*) Extracellular dye concentration of 100 μM is shown; $Y_i = 150$ mM, $\Delta G_E = -210$ mV. Intracellular dye concentration as a function of time is shown for different $V_{m,0}$: −220, −180, −140, and −100 mV. The arrow indicates increasing absolute value of the $V_{m,0}$. (*C*) Extracellular dye at 100 μM is shown; $V_{m,0} = -180$ mV, $Y_i = 150$ mM, $\Delta G_E = -210$ mV. Intracellular dye concentration as a function of time is shown for different apparent permeabilities of the membrane to the dye: 10^{-12}, $10^{-10.8}$, $10^{-9.6}$, $10^{-8.4}$, $10^{-7.2}$, 10^{-6} m/s. The arrow indicates increasing permeability. To see this figure in color, go online.

been characterized for use in *E. coli*. We start by identifying the working concentration that gives sufficiently large signal yet minimizes the membrane voltage perturbation, ΔV_m. Because we do not have access to ΔV_m directly, we grow the cells in the presence of ThT and use the growth rate as a proxy for affected ΔV_m. We also know from our model predictions that ΔV_m is context-dependent, so we perform the experiment in two different media. Fig. 3, *A* and *B* show *E. coli* growth curves in MM9 media supplemented with glucose or glycerol, respectively (see Materials and Methods for detailed media composition), and in the presence of a range of ThT concentrations. To assess the effect of different ThT concentrations in these two media, we plot growth rates, obtained from growth curves in Fig. 3, *A* and *B*, against the ThT concentration. Fig. 3 *C* demonstrates that 10 μM ThT or less does not significantly affect the growth rate in either media, and we call this concentration the maximum noninhibitory concentration (MNC). The growth rate reduction we observe for higher ThT concentrations is media-dependent (Fig. 3 *C*). The result is consistent with the finding of our model that the effect of the dye on a cell's physiology is environment-dependent. It could be caused by a different $V_{m,0}$, difference in charged permeable and nonpermeable species that achieve the $V_{m,0}$, difference in the initial membrane permeability, or any combination of these factors.

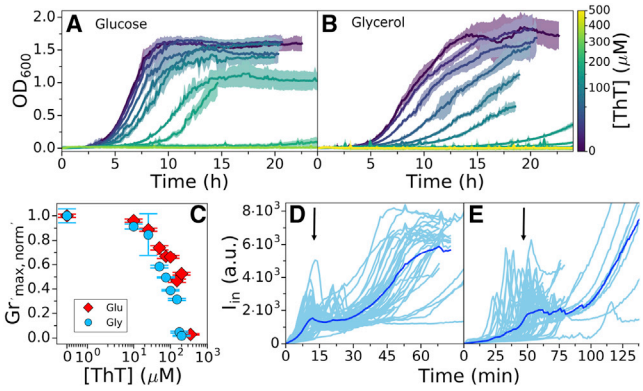

FIGURE 3 *E. coli* growth in the presence of ThT. *E. coli* growing in MM9 media supplemented with (*A*) glucose or (*B*) glycerol at increasing ThT concentration (*color map*) is shown. ThT concentrations in (*A*) are 10, 25, 50, 75, 100, 200, and 350 μM and in (*B*) are 10, 25, 50, 75, 100, 150, 175, and 200 μM. The error bars are standard deviations. (*C*) Maximum growth rates from (*A*) and (*B*) for each ThT concentration are given in red and blue, respectively. Each condition was done at least in triplicate, and error bars are the standard deviation. (*D*) I_{in} against time in LB and in (*E*) MM9 + glucose media is shown. Individual cells are shown in cyan (45 in *D* and 52 in *E* from at least nine independent experiments), and the average trace is shown in blue. The imaging conditions and $I_{ex} = 10$ μM are the same for (*E*) and (*D*). The black arrows indicate the intensity peaks. To see this figure in color, go online.

We next check that the highest ThT concentration that does not affect the growth rate (MNC), 10 μM, gives sufficiently high signal/noise ratio by observing the dye equilibration in different media. For this purpose, we no longer grow the cells in the presence of ThT (see also Materials and Methods). We note that if sufficient ΔI is achieved with 10 μM ThT, we would further check that $\Delta V_m < 1\%$ by measuring the τ_{eq} with both 10 μM and a lower dye concentration. If $\Delta V_m < 1\%$, we expect τ_{eq} not to change based on the results of our model (Fig. 2 *A*). Fig. 3 *D* shows I_{in} in time in LB, and Fig. 3 *E* shows the same in MM9 media supplemented with glucose. In both cases, fresh medium with ThT is continuously supplied using a customized flow cell (see Materials and Methods), and in both cases, ΔI is sufficiently high. However, observed profiles are different from expected (Fig. 1) and show a characteristic initial peak and a subsequent large increase that plateaus (Video S3). We reasoned that the peak could either be a real fluctuation in V_m or it could indicate an unknown dye export mechanism.

Deletion of the multidrug efflux pumps component TolC influences ThT dynamics in *E. coli*

To determine whether the observed peak in I_{in} is due to active export of the dye, we first check that in *E. coli*, ThT is not a multidrug efflux pump substrate. We are motivated by previous reports that show dyes such as ethidium bromide and Nile red are substrates of pumps belonging to the five bacterial structural families: ATP-binding

cassette, resistance/nodulation/division, multidrug and toxic compound extrusion, major facilitator superfamily, and small multidrug resistance (49–53). Fig. 4 *A* shows dye equilibration curves in a WT strain compared to the strain bearing a deletion of TolC, which is a gene encoding for an outer membrane protein that is a ubiquitous component of multidrug efflux pumps (54). The I_{in} peak in the deletion mutant did not disappear; instead, the intensity level of the peak was even higher, suggesting that the qualitative difference between the expected (Fig. 1) and the observed equilibration curve (Fig. 4 *A*) is not due to ThT export by TolC. Interestingly, in the mutant, the peak also occurred earlier in time during the loading and with less cell-to-cell variability. We next tested the effect of the ThT dye on the *ΔTolC* mutant growth rates, and for this purpose, we again grew the two strains in the presence of ThT (Fig. 4 *B*). We found that at the MNC for the WT, the mutants' growth was inhibited over the course of our experiment. Two different mechanisms could explain the results in Fig. 4: 1) ThT is a substrate of the multidrug efflux pumps or 2) membrane permeability of the TolC mutant is higher (55). In the first scenario, the strain lacking TolC accumulates more ThT than the WT (Fig. 4 *A*) and is therefore more affected by it (Fig. 4 *B*). In the second scenario, based on our model, we expect the intensity peak to appear earlier and at a higher $[Dye]_{in}$ (Fig. S12, *C* and *D*), which is what we observe in Fig. 4 *A*. We currently cannot distinguish between the two hypotheses, which could be contributing to the observed equilibration profiles at the same time.

Changing the membrane permeability during ThT loading can lead to loss of V_m

We next tested our second hypothesis, that the I_{in} peak is due to a decrease in V_m. To this end, we performed measurements of BFM speed (26) during ThT loading. The BFM is a rotary molecular motor roughly 50 nm in size that enables bacterial swimming (7) via PMF-driven rotation (56–59). The motor speed (ω) varies linearly with PMF (59,60), which enables its use as a PMF indicator and, when $pH_{in} = pH_{out}$, as a V_m indicator as well (26). In our conditions, pH_{out} is 7 and pH_{in} is 7.86 (Fig. S7), making the contribution to the PMF from ΔpH ~50 mV. Thus, even if during our experiment, ΔpH goes to 0, we can learn about the V_m behavior from the PMF measurements via the motor speed. We measure ω as before, using back-focal-plane interferometry (61) and a polystyrene bead attached to a short filament stub (see Materials and Methods) (26,30,62,63).

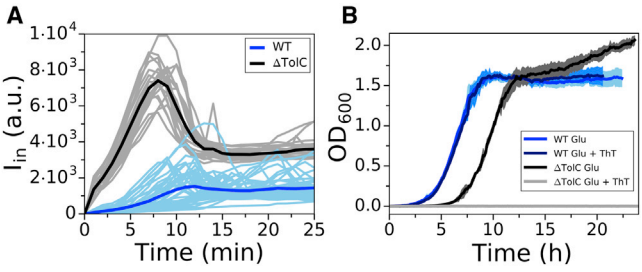

FIGURE 4 Comparison of WT and ΔTolC mutant response to ThT. (*A*) I_{in} versus time for the WT (*cyan*) and ΔTolC (*gray*) loaded in LB is shown. WT traces are reproduced from Fig. 3 *D*, and ΔTolC traces were obtained from five independent experiments to give 23 single-cell traces. Averaged traces for the WT and ΔTolC are given in blue and black, respectively. (*B*) Growth curves of WT and ΔTolC in MM9 + glucose media are given in blue (reproduced from Fig. 3 *A*) and black, respectively. Growth curves in the same media, but in the presence of 10 μM ThT, are given in cyan (WT) and gray (ΔTolC). The shaded areas show standard deviation and cyan and blue growth curves for the WT overlap. To see this figure in color, go online.

Figs. 5 *A* and S8 show simultaneous measurements of ThT intensity and normalized motor speed during dye equilibration in MM9 + glucose. The motor speed decreases during ThT equilibration, and the BFM stops at the point of the I_{in} peak. Furthermore, the BFM does not resume spinning even as I_{in} further increases, suggesting that the second ThT intensity increase that culminates in a plateau is not driven by V_m. To confirm the result, during ThT equilibration, we supplemented the medium with PI. PI permeates bacterial membrane that lost its integrity and significantly enhances its quantum yield upon binding to DNA, which is commonly interpreted as an indication of cell death (64,65). We found that the cells stained with PI, although ThT intracellular concentration remained high (Figs. 5 *B* and S9). In addition, at the time point of I_{in} decrease, cellular volume suddenly increases, and the cytoplasmically expressed fluorescent protein mCherry-mKate2 hybrid (referred to as mKate2 for brevity) (66) starts leaking out of the cell (Fig. 5 *C* and Video S4).

These results are in contradiction with our estimate of dye working concentration, and we wondered, based on Fig. 2 *C*, whether the changes in P_{Dye} could be the explanation. The cell culture in Fig. 3 was briefly exposed to light at 600 nm every 7.5 min, whereas cells in our flow cell were exposed to light of 435 nm every minute for the purpose of imaging the ThT dye. We have previously reported loss of V_m and PMF due to light-induced decrease of *E. coli* membrane's resistance at effective powers higher than ~17 mW/cm^2 and for a combination of 395 and 475 nm wavelengths (26). Light damage is wavelength-dependent (36), and we therefore characterized the light damage caused by our imaging conditions, i.e., 435 nm wavelength and effective power of P_{eff} ~ 11 mW/cm^2. Fig. S10 shows a decrease in BFMs' speed and thus the cell's PMF. However, the PMF is not fully lost, indicating that the loss of PMF observed in Fig. 5 *A* is likely caused by the combination of light-induced increase in P_{Dye} and exposure to 10 μM ThT.

To prove it, we exposed the bacteria to 10 μM ThT in LB as before, but this time, we observed the cells under bright-field illumination for 45 min, at which point we turned on

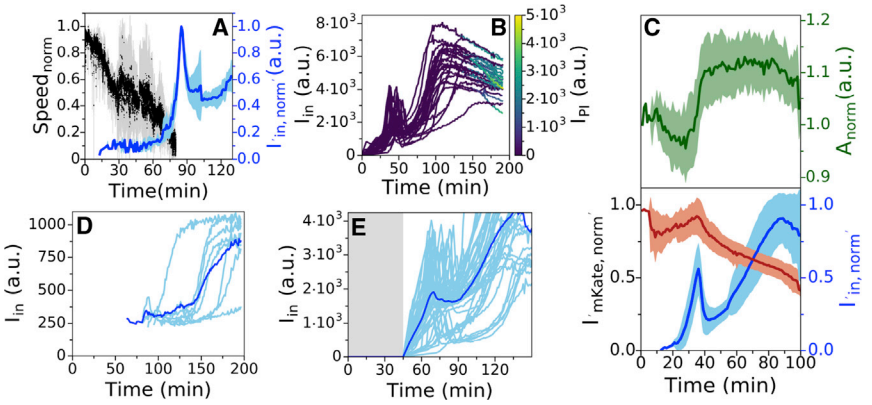

FIGURE 5 (*A*) Average traces of ThT fluorescence (in *blue*) and motor speed (in *black*) simultaneously measured in five individual cells (individual cell traces are given in Fig. S6). The shaded areas show the standard deviation, and the motor speed has been normalized to the initial value as described in Materials and Methods. (*B*) ThT (*y axes*) and PI (*color map*) equilibration profile in LB are shown. 25 individual traces are given. (*C*) Average of ThT (in *blue*), mKate2 (in *red*) fluorescence, and cell area (in *green*) simultaneously measured in 12 individual cells from three independent experiments is shown. The shaded areas show the standard deviation. (*D*) Equilibration profile of 1 μM ThT in LB is shown. Eight single-cell traces and average trace are given in cyan and blue, respectively. (*E*) Equilibration profile of 10 μM ThT in LB in the absence (*gray shaded area*) and presence of epifluorescent illumination (*light area*) is shown. The dye was flowed in the flow cell for the whole length of the experiment, and imaging conditions in the light area were the same as in Figs. 3 and 5 *D*. 44 cells from eight independent experiments are given. To see this figure in color, go online.

the 435 nm light used for epifluorescence imaging of ThT. Fig. 5 *E* shows that after 45 min, cells not exposed to 435 nm light did not take up ThT. This is in contrast to Fig. 3 *D*, in which cells exposed to 435 nm light from the start took up ThT in the first 30 min.

Actively changing membrane permeability has been used to facilitate loading of Nernstian sensors (21), and Fig. 5 *E* shows that this can change the dye into an actuator because it can influence V_m. Our mathematical model predicts that if a given concentration of the dye is lowering V_m, an even lower concentration of the dye will result in a change of τ_{eq} (Fig. S5). Because the dye equilibration profiles in Fig. 3 *D* do not follow the theoretically expected curve (Fig. 1), we cannot calculate τ_{eq}. However, from Fig. 5 *A*, we know that initial rise in the dye intensity is still driven by V_m; therefore, we can qualitatively compare the timing of the initial rise at different $[Dye]_{out}$. Fig. 5 *D* shows that for 1 μM concentration of ThT, the rise in I_{in} happens later in time than at $[Dye]_{out} = 10$ μM (Fig. 3 *D*). Thus, 10 μM ThT in LB under 435 nm light affects V_m. Assessing the suitability of the dye working concentration by confirming that a lower dye concentration does not alter τ_{eq} is a suitable additional control we propose, especially if P_{Dye} is being altered as part of the experiments.

We note that in our plate reader experiments (Fig. 2), we observed the effect of the dye (above 10 μM) on cell growth, whereas in our microscopy experiments, in the absence of light damage, ThT does not permeate WT cells. We thus wanted to confirm that at higher concentrations, ThT permeates the cells on a longer timescale, and for this purpose, we imaged the cells from the wells at representative ThT concentrations in MM9 + glucose (10, 50, and 100 μM) and MM9 + glycerol (10 μM). As expected, we found that on a longer timescale in MM9 glucose, cell brightness increases with the extracellular dye concentration, and that in MM9 + glycerol, at 10 μM, ThT signal from the cells is overall greater than in glucose (Fig. S11).

Having identified the mechanisms behind the shape of the ThT loading curve we observed in Fig. 3, we should now be able to reproduce it with our mathematical model. We focus only on the part of the equilibration curve that is V_m-driven, i.e., up to the point V_m drops to zero (as indicated in Fig. 5 *A*). Beyond, the increase in I_{in} is not driven by a Nernstian equation and thus not accounted for in our model. Based on Fig. 5 *A*, we assume that V_m decays exponentially immediately after addition of the dye (26): $V_m(t) = V_{m,0} \times 2^{t/t_{1/2}}$, where $t_{1/2}$ is the time at which voltage is half that of $V_{m,0}$. The dynamics of dye entry are then modeled by Eyring's rate law, Eq. 9, taking into account $V_{m,0}$, $t_{1/2}$, and P_{Dye} (see Supporting Materials and Methods for further details on the model). Fig. S12 shows that the model reproduces the peak in $[Dye]_{in}$ observed in Fig. 3. Immediately upon addition, the positively charged dye moves inwards because its extracellular concentration is higher than the intracellular and the cell is negatively polarized. Thus, $[Dye]_{in}$ increases and becomes greater than $[Dye]_{out}$ until the electrochemical potential reaches $\Delta G_{Dye} = 0$ (at the peak). As the V_m decays and because $[Dye]_{in} > [Dye]_{out}$, the dye now starts moving outwards, and its intracellular concentration decreases. In Fig. S12 *B*, $[Dye]_{\mathrm{in}}$ decreases to zero, whereas experimental I_{in} starts increasing after the peak and never reaches zero. The difference is explained by the fact that cells with high I_{in} after the peak are no longer viable (Fig. 5, *A* and *B*), and thus, the behavior of the dye is no longer governed with the Nernstian equation. In Fig. S12, *E* and *F*, we indicate the part of the experimental equilibration curve to which our model is applicable.

The time at which the peak occurs, as well as its intensity, depends on P_{Dye} as follows: 1) the time of the peak decreases with increasing P_{Dye} and increases with increasing $t_{1/2}$, and 2) the intensity of the peak increases with increasing P_{Dye} and $t_{1/2}$ (Fig. S9, *C* and *D*). The dye still equilibrates according to Eq. 2; however, this is achieved transiently at the time of the peak, which is the time point

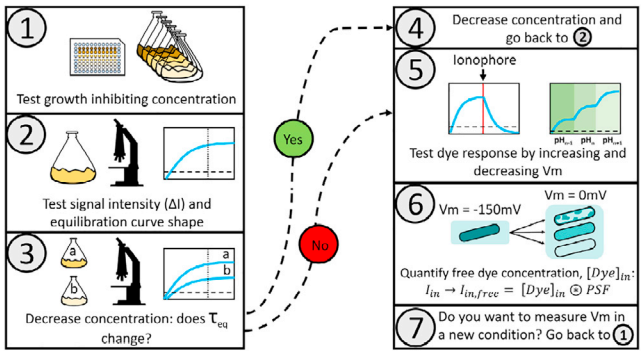

FIGURE 6 Proposed workflow for characterizing the Nernstian behavior of a candidate cationic membrane voltage dye. The working concentration is estimated in steps 1–4; we define it as the maximum dye concentration that does not affect membrane voltage and that yields sufficient amount of signal. 1) The MNC is estimated. 2) The MNC is tested for sufficient signal intensity and the shape of the equilibration profile is inspected. 3) The effect of the dye on V_m is determined by measuring τ_{eq} at different below-MNC concentrations. 4) Different τ_{eq} for different dye concentrations indicate that the probe is altering V_m and the working concentration should be reduced and the protocol resumed from step 2. Equal τ_{eq} indicates that the probe is not altering V_m. 5) Common procedures to test the expected Nernstian dye responses can then be applied, such as the introduction of a ionophore that neutralizes V_m or changes in external pH that induce changes in V_m (21). 6) I_{in} from the free dye should be separated from the I_{in} from the bound dye, and $[Dye]_{in}$ should be calculated from I_{in} by taking into account the microscope's points spread function. 7) Because the effects depend on the physiological state of the cell, the procedure should be repeated for every experimental condition. To see this figure in color, go online.

at which V_m can be calculated from Eq. 2. Because V_m varies during the course of the experiment, the V_m measured at the peak is not equal to $V_{m,0}$. Nonetheless, if we measure $V_m(t)/V_{m,0}$ as well as calculate the V_m at the time of the peak using Eq. 2, in principle, we can estimate $V_{m,0}$ as well. Therefore, charged dyes can be used to estimate initial V_m even in conditions in which they act as actuators and collapse V_m, if the dynamical shape of the V_m loss is known.

DISCUSSION

Nernstian probes are a popular choice for estimating bacterial V_m because the concentration of the free dye directly depends on V_m according to the Nernst equation. Despite the wide usage, the probes are often not sufficiently calibrated before use in different conditions. Here, we present a mathematical model that shows tradeoffs between requirements imposed on the dye: sufficient signal/noise ratio, sufficiently short dye equilibration time, and minimal effect on the cells' physiology. Based on the model results, we characterize in *E. coli* the fluorescent dye ThT, recently used in *B. subtilis* (25). Finally, we propose a general workflow for the characterization of Nernstian dye candidates (Fig. 6).

Results of our model show that the dye working concentration that does not affect V_m is context-dependent, e.g., it can be different for different external media. The model also predicts that if $\Delta V_m = 0$ at a chosen dye working concentration, lower dye concentrations should leave τ_{eq} unchanged. The finding offers a simple test to confirm the suitability of the chosen dye working concentration.

For the case of *E. coli* and ThT as the candidate Nernstian dye, we experimentally find that the dye equilibration profile does not follow the theoretical expectation (Fig. 1). We test two possible explanations for the shape of the equilibration profile we observe in Fig. 2: 1) involvement of active efflux pumps and 2) significant V_m decrease during ThT equilibration. Although we find that the strain lacking one of the efflux pumps shows a different equilibration profile when compared to the WT, it still does not behave as theoretically expected. Instead, we find that the permeability of *E. coli's* membrane to ThT is low. Permeabilizing the membrane by light of relatively short wavelengths to facilitate sufficient ThT entrance into the cell causes significant V_m reduction, which subsequently results in cell death. The finding is consistent with previous results that show that *E. coli*'s membrane needs to be permeabilized with EDTA to achieve experimentally reasonable loading times of tetramethyl rhodamine methyl ester (TMRM) dye (21). EDTA is thought to increase the permeability of *E. coli* by chelating the metal ions that cross-link the lipopolysaccharide (LPS) (67). Some evidence also suggests that it might interact directly with lipids destabilizing the membrane (68). The equilibration profiles we observe for the efflux pump mutant strain can be explained either by the change in membrane permeability between the two strains or by active efflux.

We summarize the results from our model and experiments, as well as previous work on Nernstian V_m dye usage, in a workflow (Fig. 6). We believe it is sufficiently simple and general to provide a common standard for benchmarking the cationic dye behavior and thus improve the robustness of V_m measurements. It starts with a protocol to identify the dye working concentration (Fig. 6, *steps 1–4*). This is first carried out by assaying the effect of the dye on bacterial growth, as we did in Fig. 3, *A–C*, because it is a physiological variable that is easy to measure and it will likely be affected by changes in V_m (*step 1*). In step 1, we identify the MNC as the maximum dye concentration that does not affect growth. We use it to measure the dye equilibration profile in step 2. This allows us not only to make sure that with the MNC, we are obtaining the expected shape of the equilibration profile, but also that the MNC gives sufficiently high intracellular signal. Next, we further test, as we did by comparing Figs. 3 *D* and 5 *D*, whether the MNC is affecting V_m by checking that τ_{eq} for the MNC and a chosen concentration below it stay the same (*step 3*). If the below-MNC concentration and the MNC do not show the same τ_{eq}, steps 1–3 need to be repeated for progressively lower dye concentrations until either the signal from the intracellular dye becomes too low or τ_{eq} does not differ between the two tested concentrations. In the second case, the higher concentration can be considered suitable. The next step in the workflow is more commonly performed when

assaying V_m dyes (16,21), where cells' V_m is changed in a known way, e.g., by exposing the cells to ionophores and observing V_m collapse (*step 5*). Finally, quantifying V_m requires estimation of $[Dye]_{in}$ from I_{in} measurements, which can be done by distinguishing the free from the bound dye and by taking into account that the obtained I_{in} is a convolution of $[Dye]_{in}$ and the microscope point spread function (21,23) (*step 6*). Because the dye's behavior is context-dependent, steps 1–6 should be repeated for each new experimental condition. Furthermore, if the dye fails any of the steps in the proposed workflow, it is not suitable for use as a Nernstian sensor. For example, ThT for the case of *E. coli* failed in steps 2 and 3, which is why we did not need to perform subsequent steps of the workflow.

SUPPORTING MATERIAL

Supporting Material can be found online at https://doi.org/10.1016/j.bpj.2019.10.030.

AUTHOR CONTRIBUTIONS

L.M., G.T., C.-J.L., F.B., and T.P. conceived the experiments and the computational work. L.M., T.T., Y.P., and Y.L. performed experiments. G.T. performed computational work. L.M. analyzed experimental data. L.M., G.T., C.-J.L., F.B., and T.P. interpreted the results and wrote the manuscript.

ACKNOWLEDGMENTS

We thank Dario Miroli for help with image analysis, Nathan Lord and Sebastian Jaramillo-Riveri for donating us the construct containing the hybrid mCherry-mKate2 sequence, and Angela Dawson for retrieving the ΔTolC mutant from the Keio collection.

This work was financially supported by the Cunningham Trust scholarship ACC/KWF/PhD1 to T.P. and L.M.; the National Natural Science Foundation of China under grants No. 31722003 and No. 31770925 to F.B.; the Ministry of Science and Technology, Republic of China, under contract No. MOST-107-2112-M-008-025-MY3, to C.-J.L.; and Human Frontiers Program grant RGP0041/2015 to T.P., F.B., and C.-J.L. T.P. acknowledges the support of UK Research Councils Synthetic Biology for Growth programme and is a member of the Biotechnology and Biological Sciences Research Council/Engineering and Physical Sciences Research Council/Medical Research Council-funded Synthetic Biology Research Centre (BB/M018040/1).

REFERENCES

1. Del Castillo, J., and B. Katz. 1954. Quantal components of the end-plate potential. *J. Physiol.* 124:560–573.
2. Mitchell, P. 1961. Coupling of phosphorylation to electron and hydrogen transfer by a chemi-osmotic type of mechanism. *Nature.* 191:144–148.
3. Ramos, S., and H. R. Kaback. 1977. The relationship between the electrochemical proton gradient and active transport in *Escherichia coli* membrane vesicles. *Biochemistry.* 16:854–859.
4. Bradbeer, C. 1993. The proton motive force drives the outer membrane transport of cobalamin in *Escherichia coli*. *J. Bacteriol.* 175:3146–3150.
5. Jahreis, K., E. F. Pimentel-Schmitt, …, F. Titgemeyer. 2008. Ins and outs of glucose transport systems in eubacteria. *FEMS Microbiol. Rev.* 32:891–907.
6. Wood, J. M. 2015. Bacterial responses to osmotic challenges. *J. Gen. Physiol.* 145:381–388.
7. Sowa, Y., and R. M. Berry. 2008. Bacterial flagellar motor. *Q. Rev. Biophys.* 41:103–132.
8. Strahl, H., and L. W. Hamoen. 2010. Membrane potential is important for bacterial cell division. *Proc. Natl. Acad. Sci. USA.* 107:12281–12286.
9. Bernstein, J. 1868. Ueber den zeitlichen verlauf der negativen schwankung des nervenstroms. *Pflügers Arch.* 1:173–207.
10. Hodgkin, A. L., and A. F. Huxley. 1939. Action potentials recorded from inside a nerve fibre. *Nature.* 144:710–711.
11. Neher, E., and B. Sakmann. 1976. Single-channel currents recorded from membrane of denervated frog muscle fibres. *Nature.* 260:799–802.
12. Sakmann, B., and E. Neher. 1984. Patch clamp techniques for studying ionic channels in excitable membranes. *Annu. Rev. Physiol.* 46:455–472.
13. Ling, G., and R. W. Gerard. 1949. The normal membrane potential of frog sartorius fibers. *J. Cell. Comp. Physiol.* 34:383–396.
14. Martinac, B., M. Buechner, …, C. Kung. 1987. Pressure-sensitive ion channel in *Escherichia coli*. *Proc. Natl. Acad. Sci. USA.* 84:2297–2301.
15. Martinac, B., P. R. Rohde, …, T. Nomura. 2013. Patch clamp electrophysiology for the study of bacterial ion channels in giant spheroplasts of E. coli. *Methods Mol. Biol.* 966:367–380.
16. Felle, H., J. S. Porter, …, H. R. Kaback. 1980. Quantitative measurements of membrane potential in *Escherichia coli*. *Biochemistry.* 19:3585–3590.
17. Tsutsui, H., S. Karasawa, …, A. Miyawaki. 2008. Improving membrane voltage measurements using FRET with new fluorescent proteins. *Nat. Methods.* 5:683–685.
18. Fluhler, E., V. G. Burnham, and L. M. Loew. 1985. Spectra, membrane binding, and potentiometric responses of new charge shift probes. *Biochemistry.* 24:5749–5755.
19. Kralj, J. M., D. R. Hochbaum, …, A. E. Cohen. 2011. Electrical spiking in *Escherichia coli* probed with a fluorescent voltage-indicating protein. *Science.* 333:345–348.
20. Sims, P. J., A. S. Waggoner, …, J. F. Hoffman. 1974. Studies on the mechanism by which cyanine dyes measure membrane potential in red blood cells and phosphatidylcholine vesicles. *Biochemistry.* 13:3315–3330.
21. Lo, C. J., M. C. Leake, …, R. M. Berry. 2007. Nonequivalence of membrane voltage and ion-gradient as driving forces for the bacterial flagellar motor at low load. *Biophys. J.* 93:294–302.
22. Kashket, E. R. 1985. The proton motive force in bacteria: a critical assessment of methods. *Annu. Rev. Microbiol.* 39:219–242.
23. Ehrenberg, B., V. Montana, …, L. M. Loew. 1988. Membrane potential can be determined in individual cells from the nernstian distribution of cationic dyes. *Biophys. J.* 53:785–794.
24. Te Winkel, J. D., D. A. Gray, …, H. Strahl. 2016. Analysis of antimicrobial-triggered membrane depolarization using voltage sensitive dyes. *Front. Cell Dev. Biol.* 4:29.
25. Prindle, A., J. Liu, …, G. M. Süel. 2015. Ion channels enable electrical communication in bacterial communities. *Nature.* 527:59–63.
26. Krasnopeeva, E., C. J. Lo, and T. Pilizota. 2019. Single-cell bacterial electrophysiology reveals mechanisms of stress-induced damage. *Biophys. J.* 116:2390–2399.
27. Baba, T., T. Ara, …, H. Mori. 2006. Construction of *Escherichia coli* K-12 in-frame, single-gene knockout mutants: the Keio collection. *Mol. Syst. Biol.* 2:2006.0008.
28. Datsenko, K. A., and B. L. Wanner. 2000. One-step inactivation of chromosomal genes in *Escherichia coli* K-12 using PCR products. *Proc. Natl. Acad. Sci. USA.* 97:6640–6645.

29. Pilizota, T., and J. W. Shaevitz. 2012. Fast, multiphase volume adaptation to hyperosmotic shock by *Escherichia coli*. *PLoS One.* 7:e35205.
30. Rosko, J., V. A. Martinez, …, T. Pilizota. 2017. Osmotaxis in *Escherichia coli* through changes in motor speed. *Proc. Natl. Acad. Sci. USA.* 114:E7969–E7976.
31. Rosko, J. 2017. Osmotaxis in Escherichia coli. University of Edinburgh, PhD thesis.
32. Krasnopeeva, E. 2019. Single cell measurements of bacterial physiology traits during exposure to an external stress. University of Edinburgh, PhD thesis.
33. Sulatskaya, A. I., A. V. Lavysh, …, K. K. Turoverov. 2017. Thioflavin T fluoresces as excimer in highly concentrated aqueous solutions and as monomer being incorporated in amyloid fibrils. *Sci. Rep.* 7:2146.
34. Maskevich, A. A., V. I. Stsiapura, …, K. K. Turoverov. 2007. Spectral properties of thioflavin T in solvents with different dielectric properties and in a fibril-incorporated form. *J. Proteome Res.* 6:1392–1401.
35. Maskevich, A. A., A. V. Lavysh, …, K. K. Turoverov. 2015. Spectral manifestations of thioflavin t aggregation. *J. Appl. Spectrosc.* 82:33–39.
36. Vermeulen, N., W. J. Keeler, …, K. T. Leung. 2008. The bactericidal effect of ultraviolet and visible light on Escherichia coli. *Biotechnol. Bioeng.* 99:550–556.
37. Buda, R., Y. Liu, …, T. Pilizota. 2016. Dynamics of *Escherichia coli*'s passive response to a sudden decrease in external osmolarity. *Proc. Natl. Acad. Sci. USA.* 113:E5838–E5846.
38. Wang, Y. K., E. Krasnopeeva, …, C.-J. Lo. 2019. Comparison of *Escherichia coli* surface attachment methods for single-cell, *in vivo* microscopy. *bioRxiv* https://doi.org/10.1101/648840.
39. Otsu, N. 1979. A threshold selection method from gray-level histograms. *IEEE Trans. Syst. Man Cybern.* 9:62–66.
40. Swain, P. S., K. Stevenson, …, T. Pilizota. 2016. Inferring time derivatives including cell growth rates using Gaussian processes. *Nat. Commun.* 7:13766.
41. Rybak, S. L., F. Lanni, and R. F. Murphy. 1997. Theoretical considerations on the role of membrane potential in the regulation of endosomal pH. *Biophys. J.* 73:674–687.
42. Grabe, M., and G. Oster. 2001. Regulation of organelle acidity. *J. Gen. Physiol.* 117:329–344.
43. Nelson, P. 2003. Biological Physics: Energy, Information, Life. W. H. Freeman, New York.
44. Keener, J., and J. Sneyd. 2009. Mathematical Physiology, Second Edition. Springer, Berlin, Germany.
45. Garlid, K. D., and P. Paucek. 2003. Mitochondrial potassium transport: the k(+) cycle. *Biochim. Biophys. Acta.* 1606:23–41.
46. Garlid, K. D., A. D. Beavis, and S. K. Ratkje. 1989. On the nature of ion leaks in energy-transducing membranes. *Biochim. Biophys. Acta.* 976:109–120.
47. Shinoda, W. 2016. Permeability across lipid membranes. *Biochim. Biophys. Acta.* 1858:2254–2265.
48. Goldman, D. E. 1943. Potential, impedance, and rectification in membranes. *J. Gen. Physiol.* 27:37–60.
49. Alvarez-Ortega, C., J. Olivares, and J. L. Martínez. 2013. RND multidrug efflux pumps: what are they good for? *Front. Microbiol.* 4:7.
50. Lubelski, J., W. N. Konings, and A. J. M. Driessen. 2007. Distribution and physiology of ABC-type transporters contributing to multidrug resistance in bacteria. *Microbiol. Mol. Biol. Rev.* 71:463–476.
51. Nikaido, H., and Y. Takatsuka. 2009. Mechanisms of RND multidrug efflux pumps. *Biochim. Biophys. Acta.* 1794:769–781.
52. Kuroda, T., and T. Tsuchiya. 2009. Multidrug efflux transporters in the MATE family. *Biochim. Biophys. Acta.* 1794:763–768, Published online December 6, 2008.
53. Bay, D. C., K. L. Rommens, and R. J. Turner. 2008. Small multidrug resistance proteins: a multidrug transporter family that continues to grow. *Biochim. Biophys. Acta.* 1778:1814–1838.
54. Anes, J., M. P. McCusker, …, M. Martins. 2015. The ins and outs of RND efflux pumps in *Escherichia coli*. *Front. Microbiol.* 6:587.
55. Dhamdhere, G., and H. I. Zgurskaya. 2010. Metabolic shutdown in *Escherichia coli* cells lacking the outer membrane channel TolC. *Mol. Microbiol.* 77:743–754.
56. Manson, M. D., P. M. Tedesco, and H. C. Berg. 1980. Energetics of flagellar rotation in bacteria. *J. Mol. Biol.* 138:541–561.
57. Matsura, S., J. Shioi, and Y. Imae. 1977. Motility in Bacillus subtilis driven by an artificial protonmotive force. *FEBS Lett.* 82:187–190.
58. Meister, M., and H. C. Berg. 1987. The stall torque of the bacterial flagellar motor. *Biophys. J.* 52:413–419.
59. Fung, D. C., and H. C. Berg. 1995. Powering the flagellar motor of Escherichia coli with an external voltage source. *Nature.* 375:809–812.
60. Gabel, C. V., and H. C. Berg. 2003. The speed of the flagellar rotary motor of *Escherichia coli* varies linearly with protonmotive force. *Proc. Natl. Acad. Sci. USA.* 100:8748–8751.
61. Svoboda, K., C. F. Schmidt, …, S. M. Block. 1993. Direct observation of kinesin stepping by optical trapping interferometry. *Nature.* 365:721–727.
62. Ryu, W. S., R. M. Berry, and H. C. Berg. 2000. Torque-generating units of the flagellar motor of *Escherichia coli* have a high duty ratio. *Nature.* 403:444–447.
63. Bai, F., R. W. Branch, …, R. M. Berry. 2010. Conformational spread as a mechanism for cooperativity in the bacterial flagellar switch. *Science.* 327:685–689.
64. López-Amorós, R., J. Comas, and J. Vives-Rego. 1995. Flow cytometric assessment of *Escherichia coli* and *Salmonella typhimurium* starvation-survival in seawater using rhodamine 123, propidium iodide, and oxonol. *Appl. Environ. Microbiol.* 61:2521–2526.
65. Krämer, C. E., W. Wiechert, and D. Kohlheyer. 2016. Time-resolved, single-cell analysis of induced and programmed cell death via non-invasive propidium iodide and counterstain perfusion. *Sci. Rep.* 6:32104.
66. Lord, N. D. 2014. Fluctuation timescales in bacterial gene expression. Harvard University, PhD thesis.
67. Vaara, M. 1992. Agents that increase the permeability of the outer membrane. *Microbiol. Rev.* 56:395–411.
68. Prachayasittikul, V., C. Isarankura-Na-Ayudhya, …, H. J. Galla. 2007. EDTA-induced membrane fluidization and destabilization: biophysical studies on artificial lipid membranes. *Acta Biochim. Biophys. Sin. (Shanghai).* 39:901–913.